Available online at www.sciencedirect.com
ScienceDirect
Trans. Nonferrous Met. Soc. China 35(2025) 1890−1906
Transactions of Nonferrous Metals Society of China
www.tnmsc.cn

Tailoring microstructure, tensile properties, and creep resistance of additively manufactured Inconel 718 superalloy by post heat treatment

Sajad GHAEMIFAR[1], Milad ROOSTAEI[2,3], Mohammad REZA ZAMANI[1], Stefan WURSTER[2], Hamed MIRZADEH[1]

1. School of Metallurgy and Materials Engineering, College of Engineering, University of Tehran, Tehran, Iran;
2. Erich Schmid Institute of Materials Science, Austrian Academy of Sciences, Jahnstraße 12, 8700 Leoben, Austria;
3. Department of Materials Science, Chair of Materials Physics, Montanuniversität Leoben, 8700 Leoben, Austria

Received 21 December 2023; accepted 7 August 2024

Abstract: The effects of post heat treatment on the microstructure, aging kinetics, and room/elevated temperature mechanical properties of additively manufactured Inconel 718 superalloy were investigated. Scanning electron microscopy (SEM), electron backscattered diffraction (EBSD), and X-ray diffraction (XRD), as well as hardness, tensile, and creep testing were used for characterization. At temperatures higher than 1100 °C, homogenization treatment resulted in the appearance of equiaxed grains by recrystallization and diminishing the dislocation density. The precipitation activation energy for the homogenized and aged condition was obtained as 203.2 kJ/mol, which was higher than the value of ~160 kJ/mol for the as-built IN718 superalloy. Therefore, direct aging resulted in a faster aging response, which led to a significant improvement in tensile properties, as rationalized by the strengthening mechanisms. Direct aging treatment resulted in a higher elevated-temperature ultimate tensile strength (UTS) as well as the optimum creep life and the lowest minimum creep rate in comparison with other heat treatment routes, which were attributed to the presence of fine and uniformly dispersed strengthening precipitates in conjunction with the high dislocation density.

Key words: Inconel 718 superalloy; additive manufacturing; post heat treatment; mechanical properties; creep resistance

1 Introduction

As an emerging manufacturing method, additive manufacturing (AM) has attracted considerable attention for producing high tech metallic materials, especially those with complex geometry [1−3]. Powder bed fusion (PBF) [4,5] and directed energy deposition (DED) [6,7] are the most well-known methods for the fabrication of metallic parts, where various energy sources such as laser beam, electron beam, and electric arc can be used. For instance, laser powder bed fusion (L-PBF) is one of the most widely utilized methods for the fabrication of parts with proper mechanical properties [8,9]. On the other hand, due to the nature of these methods which usually result in some defects or undesirable features in the as-built microstructure [10,11], adopting the post processing treatments plays a crucial role in obtaining desirable microstructure as well as properties [12,13].

Ni-based superalloys are known as materials for high temperature applications, which are used in various industries such as power generation, aerospace, and petroleum [14,15]. As an illustration, owing to its desirable mechanical properties [16], proper oxidation resistance [17], and good weldability [18], Inconel 718 (IN718) superalloy is

Corresponding author: Hamed MIRZADEH, E-mail: hmirzadeh@ut.ac.ir
https://doi.org/10.1016/S1003-6326(25)66789-6

widely used in aforesaid industries. In this regard, AM methods, especially the L-PBF, have been recently used for manufacturing IN718 parts, in which the favorable weldability of IN718 is important for manufacturability [19].

The importance of post processing in additively manufactured IN718 has been reported in recent studies [20]. As stated in previous studies [21], IN718 is also known as an age hardening superalloy owing to its potential for the formation of strengthening precipitates such as γ' and γ'' during aging treatments. Moreover, Laves and δ phases are reported phases in the micro-structure of this superalloy [22]. It should be noted that the presence of the Laves phase, as a result of micro-segregation during solidification, leads to the deterioration of mechanical properties [23] and can be dissolved during solution/homogenization treatments to provide an appropriate aging response [24]. Furthermore, the importance of the heat treatment parameters (i.e. time and temperature) has been investigated through the kinetics analysis of the Laves phase dissolution [25] and the NbC carbide precipitation [26]. It has been revealed that these parameters have a significant effect on the obtained microstructure. Hence, performing post heat treatment as a post processing route for the additively manufactured IN718 has a significant effect on its final microstructure as well as mechanical properties. The effect of post heat treatments on the mechanical properties of additively manufactured IN718 has been shown in previous works [8,24]. With the approach of process−structure−property relationships, GALLMEYER et al [27] showed that the solution annealing at 1020 °C for 15 min, followed by aging at 720 °C for 24 h results in optimum room temperature tensile properties. On the other hand, HUANG et al [28] reported that performing aging treatment directly from the as-built condition leads to a superior ultimate tensile strength (UTS) of 1545 MPa; while the existence of the Laves phase results in inappropriate elongation to failure of 14.1%. Moreover, the effect of standard heat treatment on the creep resistance of IN718 superalloy manufactured by the L-PBF method has been studied and it has been stated that the recommended microstructure for optimal creep performance includes large equiaxed grains, elimination of texture, dissolution of Laves and δ phases, and the precipitation of fine carbides and γ'' precipitates [29].

While there are some reported works [27−29] on the effect of post processing and heat treatments on the mechanical properties of IN718 superalloy manufactured by the L-PBF method, unveiling the microstructural evolution as well as performing a wide range of heat treatments to obtain the process−microstructure−property relationship needs more investigations. Moreover, a comprehensive study of the room and high temperature tensile properties as well as the creep behavior for various heat treated additively manufactured IN718 superalloys is needed, where their relations to the microstructure and underlying mechanisms should be further studied. Accordingly, the present study is dedicated to achieve these aims via investigating the effect of post heat treatments on the aging kinetics to obtain optimum temperature and time of heat treatments, and consequently, optimizing the room and elevated temperature mechanical properties.

2 Experimental

Figures 1(a) and (b) show the gas atomized IN718 powders (EOS NickelAlloy IN718) with particle diameters in the range of 15−50 μm, which have been used for the fabrication process. The L-PBF process was performed with a laser power of 95 W, scanning speed of 800 mm/s, hatching distance of 0.05 mm, layer thickness of 0.025 mm, and scanning strategy of stripe/67° to produce samples. More details of the fabrication process can be found elsewhere [25].

The homogenization treatment was performed at temperatures in the range from 1050 to 1150 °C for durations from 5 min to 10 h; while the aging treatment was performed at temperatures from 700 to 850 °C for durations from 5 min to 8 h. It should be noted that all heat treatments in this study were carried out in a muffle furnace with the heating rate of 10 °C/min and precision of ±2 °C. Moreover, the time counting of each heat treatment cycle was started at the moment that temperature reaches the pre-determined value. Furthermore, all specimens were water-quenched directly to preserve the elevated-temperature microstructure and prevent any undesired phase transformation. The samples were etched with Kalling's 2 solution. Afterwards, a field-emission scanning electron microscope

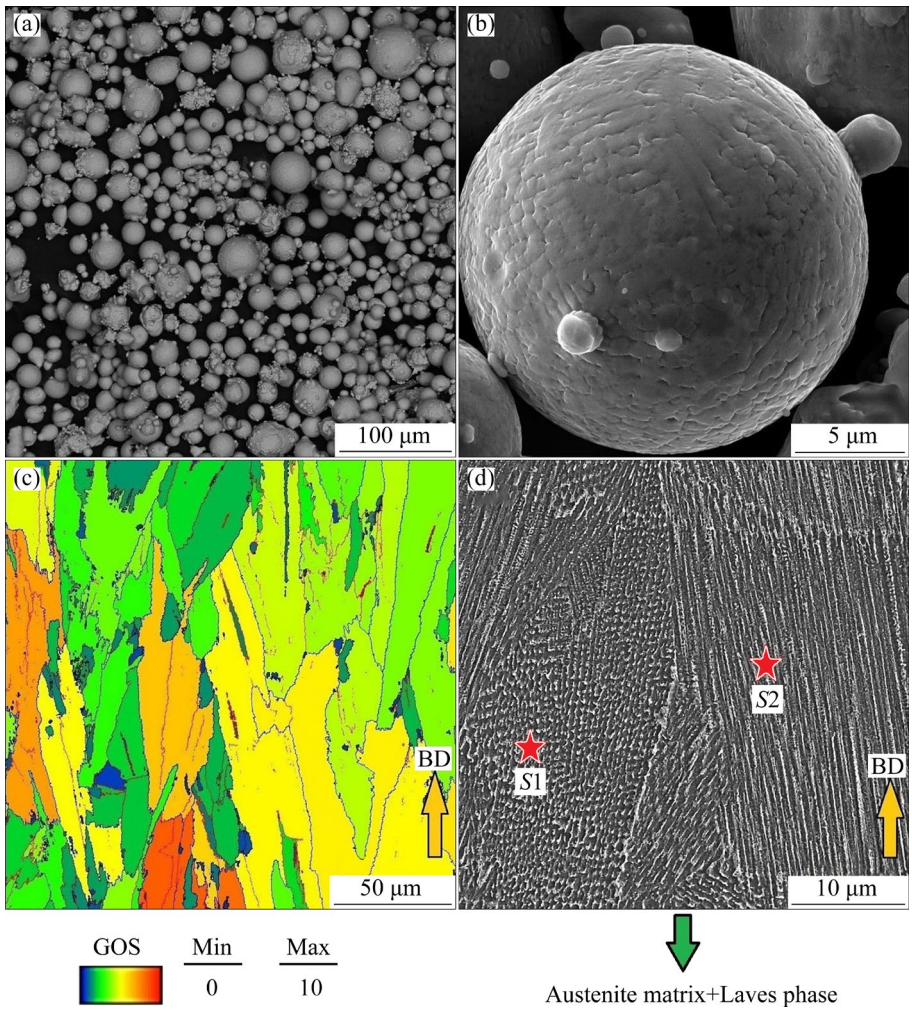

Fig. 1 (a, b) SEM images of atomized powder particles; (c) Grain orientation spread (GOS) map; (d) SEM image of as-built sample (*S*1 and *S*2 are EDS examined points; BD: Building direction)

(MIRA3 TESCAN FESEM) was adopted for the microstructure observation. Moreover, an EDS detector was used for the elemental analysis and spectra were analyzed using ZAF correction. Following grinding and vibratory polishing with alumina and colloidal silica, the electron backscatter diffraction (EBSD) examination was performed using a Tescan Magna FESEM coupled with a Bruker e$^-$-Flash^{FS} EBSD detector. ATEX [30] and orientation imaging microscopy (OIM) softwares were used to evaluate the obtained EBSD scans. Post-processing was carried out by removing points with a confidence index lower than 0.1.

The Vickers indentation test was utilized for the hardness measurements with a load of 5 kg, in which at least five indentations were averaged. The horizontally oriented (perpendicular to the building direction) tensile and creep test samples were based on the ASTM E8 standard. It should be noted that the flat test specimens with the gauge length of 25 mm, gauge width of 6 mm, and gauge thickness of 1 mm were used for these mechanical testing. The tensile and creep tests were conducted at room temperature and 650 °C (which has been stated as the working temperature [31]), respectively. The creep tests were performed under the stress of 700 MPa. It is noteworthy to state that the creep test was performed according to the test procedure, which has been mentioned in the ASTM E139 standard. Moreover, the crosshead speed of tensile testing was set at 0.6 mm/min (initial strain rate of 4×10^{-4} s^{-1}) for both room temperature and elevated temperature tensile tests, and these tests were performed by a SANTAM universal testing machine, which was equipped with a muffle furnace and extensometer. To guarantee the reproducibility

of heat treatment processes, each of mechanical tests was repeated at least 3 samples. X-ray diffraction (using a PHILIPS diffractometer with Cu K_α radiation) was performed for the phase identification a scan rate of 2 (°)/min.

3 Results and discussion

3.1 Microstructural evolution during homogenization

The grain orientation spread (GOS) map of the as-built sample is shown in Fig. 1(c), where the columnar grains can be seen. Moreover, these grains show a high value of GOS (higher than 1°), which implies that these grains are unrecrystallized. This is related to the high cooling rate during L-PBF, which results in the development of local strain inhomogeneity and accordingly a high dislocation density [32,33]. The SEM image of the as-built sample in Fig. 1(d) shows that the microstructure consists of the matrix and a bright phase, which is present in two distinct forms of cellular (Point *S*1) and columnar (Point *S*2) morphology. As shown in Table 1, both Points *S*1 and *S*2 are consistent with the Ni/Nb molar ratio of ~2. While EDS analysis might not be accurate and the EDS spectrum might be influenced by etching and the matrix can also take part in the results, the EDS analysis was performed at high magnifications with a focused beam to get more accurate outcomes. The Ni/Nb molar ratio of ~2 is consistent with the Ni_2Nb phase, similar to other investigations [34].

Table 1 EDS analysis results of samples

Analyzed spot	Content/at.%								Ni/Nb molar ratio
	Ni	Cr	Nb	Mo	Ti	Al	Fe	C	
*S*1	32.1	23.4	16.5	1.1	1.3	9.5	16.1	–	1.95
*S*2	32.9	23.1	16.2	1.4	1.4	8.9	16.1	–	2.03
*S*3	15.3	1.4	26.3	1.3	3.2	1.5	1.1	49.9	–
*S*4	36.1	23.6	11.6	1.5	1.2	9.7	16.3	–	3.11
*S*5	35.5	23.8	11.4	1.3	1.5	10.1	16.4	–	3.11
*S*6	35.7	23.6	11.1	1.5	1.4	9.9	16.8	–	3.22

The hardness values of the samples homogenized at various temperatures and time are depicted in Fig. 2. It can be seen that the homogenization treatment results in a fast decrease of hardness at all temperatures as well as a lower absolute value. For instance, the hardness of the sample homogenized at 1150 °C for 1 h is decreased from HV 336 (as-built condition) to HV 203; while the hardness values for 1 h homogenization at 1050 and 1100 °C are HV 274 and HV 260, respectively. The hardness of samples homogenized at 1150 °C for durations longer than 1 h remains nearly unchanged (HV 197 for 10 h homogenized sample), which reveals that the major microstructural evolutions have already occurred in the first 1 h of the homogenization process. Moreover, the hardness continues to decrease to HV 212 after 10 h homogenization at 1100 °C, which is close to the obtained hardness after 1 h homogenization treatment at 1150 °C (HV 203). Furthermore, the fall of hardness at 1050 °C is far less pronounced and a high hardness is retained even after 10 h. These findings should be rationalized by the microstructural analysis.

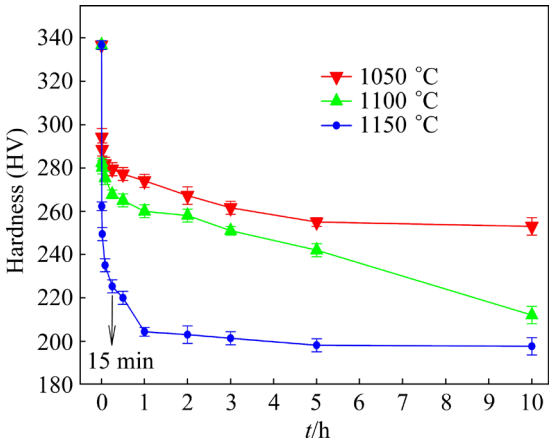

Fig. 2 Hardness evolution of samples homogenized at different temperatures

The EBSD maps and SEM images of the homogenized samples at 1150 °C for durations of 15 min, 1 h, and 10 h are represented in Fig. 3. The EBSD results of the sample homogenized at 1150 °C for 15 min show a columnar grain structure similar to the as-built microstructure, while a few fine and equiaxed grains can also be recognized (Fig. 3(a)), corresponding to the regions with low GOS (blue color) that indicate the onset of recrystallization [32]. However, still a strong columnar texture along the BD can be seen, similar to the as-built condition seen in other works [35]. The SEM image of this sample in Fig. 3(a) reveals that the Laves phase has completely dissolved, which is consistent with the previous work [25].

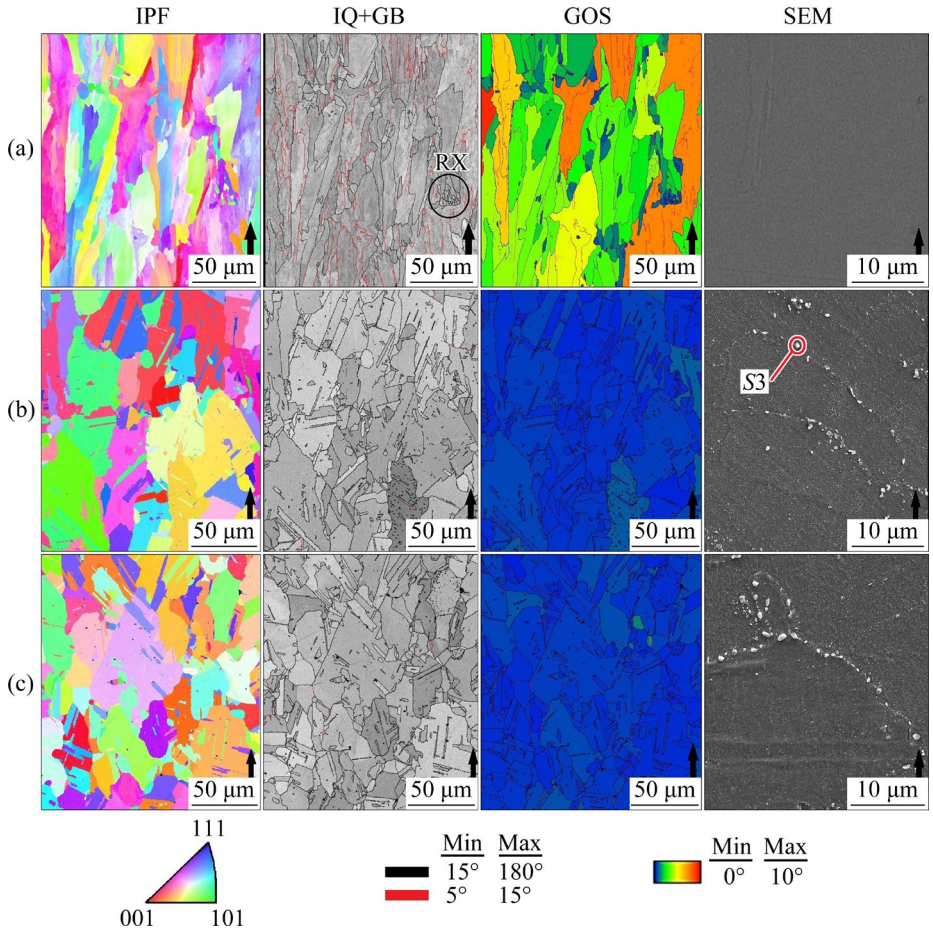

Fig. 3 EBSD maps and SEM images of samples homogenized at 1150 °C for durations of 15 min (a), 1 h (b), and 10 h (c) (BD is shown by black arrows; IPF, IQ, GB, and GOS stand for the inverse pole figure, image quality, grain boundary, and grain orientation spread, respectively)

On the other hand, after 1 h homogenization, the columnar grains change into the equiaxed grains, which depicts that recrystallization is almost completely occurred (Fig. 3(b)). The removal of columnar grain texture with the appearance of grains with different orientations (different colors according to the IPF maps) is obvious, leading to a random texture in the homogenized sample. The corresponding GOS map reveals the presence of equiaxed grains with GOS<1°, confirming the occurrence of recrystallization. Based on the SEM image of this sample (Fig. 3(b)) and the corresponding EDS analysis of Point *S*3 in Table 1, NbC carbides have appeared in the microstructure, which is consistent with the previous work [26]. The occurrence of recrystallization and dissolution of the Laves phase are responsible for the decrement of hardness during homogenization (Fig. 2). Moreover, the decrease in the dislocation density can also be indicated [36], which can be confirmed based on the popularity of the low-angle grain boundaries in the grain boundary map of 1 h (Fig. 3(b)) compared to that of 15 min (Fig. 3(a)). Furthermore, the GOS map results also confirm the mentioned reduction of dislocation density. After 10 h homogenization, the microstructure has not changed extensively, as shown in Fig. 3(c). For instance, the average grain size after 10 h annealing is 28 μm, which is comparable to 32 μm for the sample homogenized for 1 h. This reveals that the grain growth is sluggish in this material, which can be attributed to the presence of grain boundary carbides that slow down the migration of grain boundaries [37].

The EBSD maps of the samples homogenized at 1100 °C for durations of 1 and 10 h are shown in Figs. 4(a) and (b), respectively. It can be seen that 1 h homogenization time is not enough to replace the columnar grain structures with the equiaxed ones (Fig. 4(a)); while a few recrystallized grains

can be seen. However, after 10 h homogenization, a nearly equiaxed recrystallized microstructure can be seen in Fig. 4(b), which confirms the fall of hardness in Fig. 2. This reveals that the kinetics of recrystallization is much slower at 1100 °C compared to that at 1150 °C.

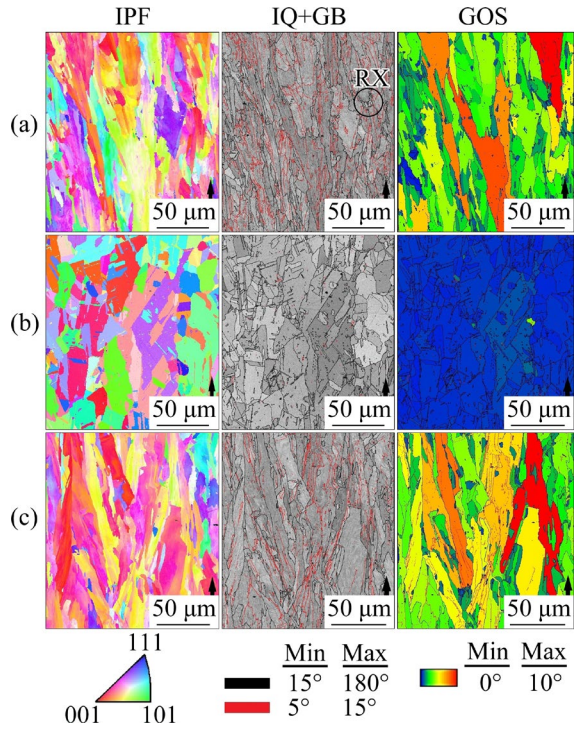

Fig. 4 EBSD maps of samples homogenized at 1100 °C for 1 h (a), 1100 °C for 10 h (b), and 1050 °C for 10 h (c) (BD is shown by black arrows)

In fact, it has been reported that performing homogenization at temperatures higher than 1100 °C leads to the occurrence of recrystallization [38], and hence, the temperature of 1100 °C seems to be the lower temperature for the occurrence of recrystallization. The EBSD maps of the sample homogenized at 1050 °C for 10 h can be consulted (Fig. 4(c)), which reveal the retention of the columnar grains up to long holding time. Therefore, it can be concluded that for the occurrence of recrystallization at reasonable time, $T \geq 1100$ °C is needed.

3.2 Microstructural evolution during aging

In the previous section, it was revealed that homogenization treatment at 1150 °C for 1 h resulted in an equiaxed microstructure as a consequence of recrystallization. Moreover, the disappearance of the Laves phase was also observed, leading to the increased Nb content of the matrix, and hence, the material is ready to be aged. The evolution of the hardness during aging treatment of the sample homogenized at 1150 °C for 1 h is depicted in Fig. 5. For each temperature, the hardness increases up to the peak-aged condition, and then decreases during overaging.

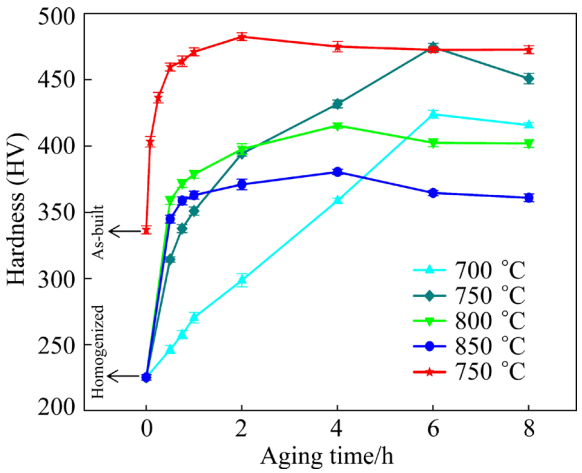

Fig. 5 Evolution of hardness of as-built as well as homogenized samples (1150 °C for 1 h) during aging at different temperatures

The EBSD maps and SEM image of the peak-aged sample at 750 °C for 6 h are represented in Fig. 6(a). The EBSD maps are similar to those of the corresponding homogenized sample (Fig. 3(b)); while the SEM image reveals the formation of disc-shaped precipitates, where the EDS analysis of Points *S*4 and *S*5 in Table 1 reveals that these precipitates are Nb-rich, and as the EDS spectra might be affected by the matrix due to the small size of the precipitates, the molar ratio of Ni/Nb is roughly 3. Therefore, Points *S*4 and *S*5 are expected to be related to the Ni_3Nb γ'' phase, which is the expected strengthening phase in the IN718 superalloy [39]. Therefore, the sharp increase in hardness in Fig. 5 is related to the formation of the precipitating phase. For comparison, the as-built sample was also peak-aged at 750 °C for 2 h as shown in Fig. 5, which resulted in a slightly higher peak hardness of HV 482 compared to HV 474 for the homogenized and aged sample.

The EBSD maps and SEM image of the peak-aged as-built sample at 750 °C for 2 h are represented in Fig. 6(b). The EBSD maps are similar to those of the as-built sample (Figs. 1(c) and (d)); while the SEM image reveals the formation of finer and more homogeneously dispersed

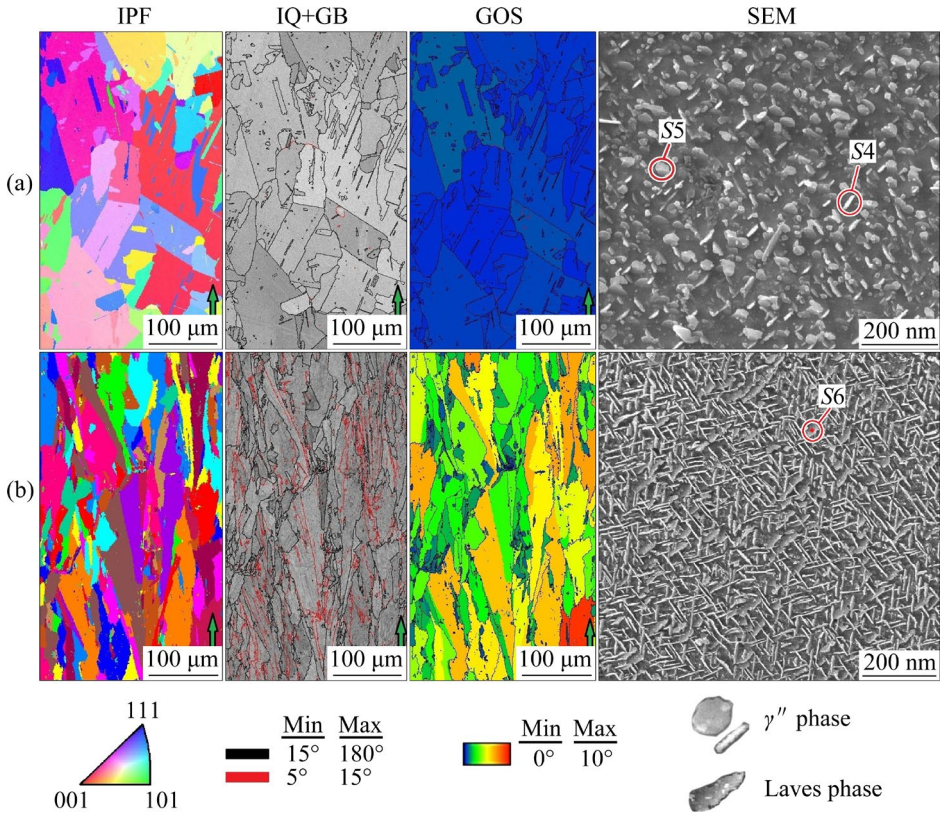

Fig. 6 EBSD maps of homogenized and aged (a) and directly aged (b) samples (Aging conditions are 750 °C for 6 h (a) and 2 h (b), respectively; BD is shown by green arrows)

disc-shaped precipitates, which can be related to the high dislocation density of the as-built sample that is conducive to the formation of precipitates. This is responsible for good age hardening response of this sample. Therefore, it can be deduced that direct aging of the as-built sample leads to a better age hardening response and a much faster rise in hardness, as can be seen in Fig. 5. Therefore, it is interesting to compare the precipitation kinetics for the two cases of as-built and homogenized conditions.

3.3 Aging kinetics

If H_0, H_{max}, and H represent the hardness of the unaged sample, peak-aged sample, and the current sample at time t, respectively, the equation of $X=(H-H_0)/(H_{max}-H_0)$ gives the transformed fraction (X). The Johnson−Mehl−Avrami−Kolmogorov (JMAK) analysis based on $X=1-\exp[-(kt)^n]$ was used for kinetics analysis [25,40,41], where n is the Avrami exponent, and k is a temperature-dependent parameter expressed by $k=k_0\exp[-Q/(RT)]$, where k_0 is a constant, and Q is the activation energy of the process. By taking the natural logarithm from the JMAK formula, the slope and the intercept of the plot of $\ln\ln[1/(1-X_H)]$ vs $\ln t$ gives the values of n and $n\ln k$, respectively, as shown in Fig. 7(a) with the linear regression results.

The Avrami exponent n was determined to be 0.66 on average, and then, the k values were obtained. Now, the slope of the plot of $\ln k$ vs $1000/(RT)$ in Fig. 7(b) was used to obtain Q=203.2 kJ/mol, which is consistent with the value of 201.7 kJ/mol for the diffusion of Nb in Ni [42]. It has been reported that the activation energy of the γ'' precipitation in the wrought IN718 is 209.2 kJ/mol [43], which is close to the obtained value in this study. This can be attributed to the stoichiometry of the γ'' phase (Ni_3Nb), which reveals that the diffusion of Nb controls the formation of the γ'' phase. In this respect, the activation energy for the diffusion of Nb in IN718 superalloy fabricated by L-PBF has been obtained to be ~160 kJ/mol, which was ascribed to the high dislocation density in the as-built condition [25]. This difference between the mentioned activation energy values can be explained by the aforesaid fact that direct aging of the as-built sample results in a

better age hardening response. In other words, due to the high dislocation density which exists in the as-built sample, reaching the peak-aged condition will be facilitated through direct aging; while homogenization leads to recrystallization as well as diminishing the dislocation density, and consequently the required time and activation energy for reaching the peak-aged condition will be increased.

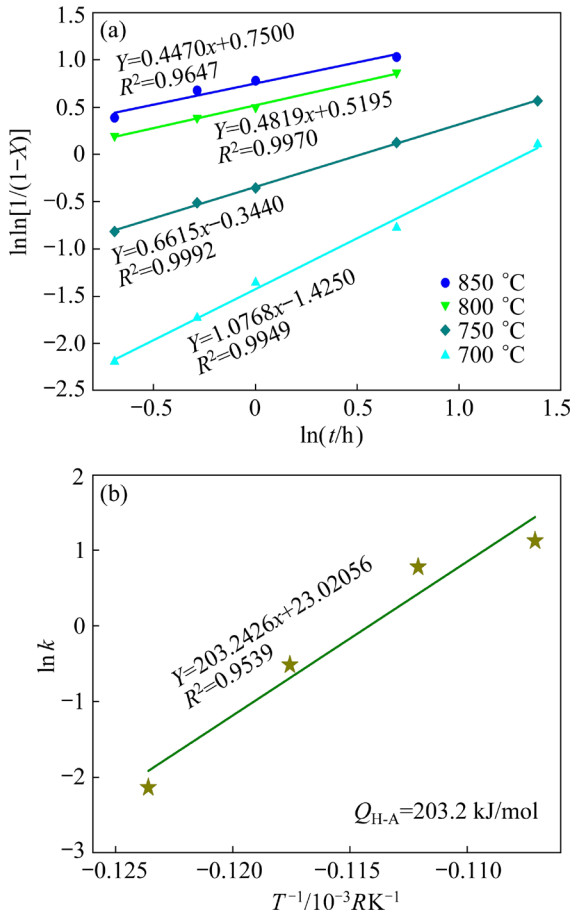

Fig. 7 Plots used for obtaining Avrami exponents (a) and activation energy (b)

3.4 Room-temperature mechanical properties

The room temperature stress−strain curves of the as-built sample, the sample homogenized at 1150 °C for 1 h, peak-aged sample from homogenized condition (aging at 750 °C for 6 h), and peak-aged sample directly from as-built condition (aging at 750 °C for 2 h) are illustrated in Fig. 8. It can be seen that the (0.2% proof) yield stress (YS) and the ultimate tensile strength (UTS) of the as-built sample are 880 and 987 MPa, respectively. There is a weak work-hardening behavior, which is similar to the results reported by ZHAO et al [44] for the same alloy. In other relevant works done by MCLOUTH et al [45] and ZHOU et al [46], while better work-hardening behaviors can be seen, the work-hardening is still inferior compared to the competitive alloys such as austenitic stainless steels with lower yield stresses that take advantage of the induced plasticity mechanisms such as transformation-induced plasticity (TRIP) effect [47].

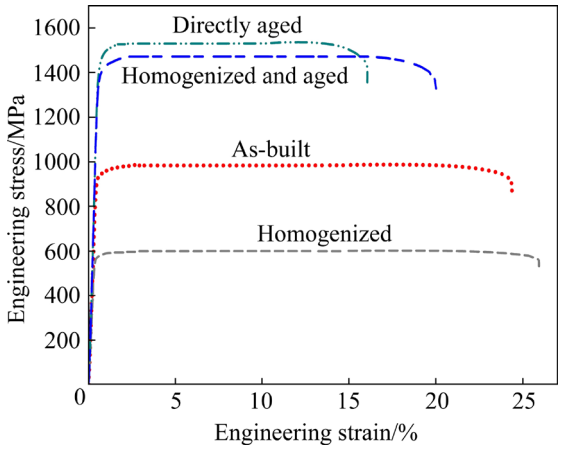

Fig. 8 Room-temperature engineering stress−strain curves of different samples

However, homogenization treatment resulted in a decrease in the YS and UTS of 560 and 601 MPa, respectively, which are attributed to the Laves phase dissolution [48], occurrence of recrystallization [36], and diminishing dislocation density [27]. Moreover, it can be seen that the aging treatment of both as-built and homogenized samples leads to an increase in the YS and UTS, in which the YS and UTS for the homogenized and aged sample are 1325 and 1473 MPa, respectively; while the YS and UTS for the directly aged sample are 1403 and 1536 MPa, respectively. This strengthening can be attributed to the formation of the strengthening γ'' phase. However, owing to the existence of the high dislocation density in the directly aged sample, the YS and UTS are higher than those in the homogenized sample. The YS and UTS for wrought IN718 after aging treatment are reported to be 978 and 1216 MPa, respectively [49]. These values are lower than the corresponding values for the aged samples in the present work and similar works based on additive manufacturing [28], which reveals that the route of additive manufacturing and aging is a viable route for the fabrication of parts with good mechanical properties.

3.5 Strengthening mechanisms

The yield strength of IN718 can be rationalized by considering various strengthening mechanisms. These mechanisms include the intrinsic strength (σ_0) of pure nickel, grain boundary strengthening ($\Delta\sigma_{GB}$), dislocation strengthening ($\Delta\sigma_d$), solid solution strengthening ($\Delta\sigma_{ss}$), and precipitation strengthening ($\Delta\sigma_p$). In the following sections, the contribution of each strengthening mechanism is quantified for the as-built, homogenized, directly aged, and homogenized and aged samples.

3.5.1 Intrinsic strength

The intrinsic strength can be calculated based on Eq. (1) [50]:

$$\sigma_0=\bar{M}\tau_{CRSS} \quad (1)$$

where $\bar{M}$ is the average Taylor factor and τ_{CRSS} refers to the critical resolved shear stress. The average Taylor factor for each sample can be obtained from Fig. 9. Furthermore, the critical resolved shear stress τ_{CRSS} for the nickel-based superalloy was set to be 17.5 MPa [50]. The calculated intrinsic strengths for each type of sample are as follows: 50.1 MPa for the as-built condition, 52.15 MPa for the homogenized condition, 51.8 MPa for the directly aged condition, and 49.35 MPa for the homogenized and aged condition.

3.5.2 Grain boundary strengthening

According to the Hall−Petch term of $710/D^{1/2}$ [51], the contribution of grain boundaries in the strength of samples can be calculated. In this equation, D represents the effective grain size. In other words, it is defined as the distance between grain boundaries that are perpendicular to the loading direction. The effective grain sizes for the specimens are as follows: 15.8 μm for the as-built specimen, 23.6 μm for the homogenized specimen, 22.5 μm for the directly aged specimen, and 28.2 μm for the homogenized and aged specimen; these grain sizes result in grain boundary strengthening of 179, 146, 150, and 134 MPa, respectively.

3.5.3 Dislocation strengthening

To determine the contribution of dislocation strengthening to yield strength, Eq. (2) was used [52]:

$$\Delta\sigma_d=\alpha\bar{M}\mu b\sqrt{\rho} \quad (2)$$

where α is 0.2 for the FCC crystal structure, μ refers to the shear modulus, which is measured to be 76 GPa for the IN718 material [44,49], b represents the magnitude of the Burgers vector (0.248 nm for IN718 [48,53]), and ρ refers to the dislocation density. A rough estimate of dislocation density can be derived based on the micro-strain (ε), according to Eq. (3) [52]. In this regard, the determination of micro-strain can be achieved using the Williamson−Hall method expressed by Eq.(4) [52]:

$$\rho=2\sqrt{3}\varepsilon/(bD) \quad (3)$$

$$\beta\cos\theta=K\lambda/D+(4\sin\theta)\varepsilon \quad (4)$$

where θ denotes the Bragg angle, K is a constant (~0.9), and λ(=0.15405 nm) stands for the wavelength of Cu K_α radiation [52]. By taking into account the XRD data presented in Fig. 10 and using Eq. (4), the micro-strain values of 0.31, 0.009, 0.175, and 0.133 were determined for the as-built, homogenized, directly aged, and homogenized and aged samples, respectively. Hence, by employing Eq. (3), the dislocation density values for the as-built,

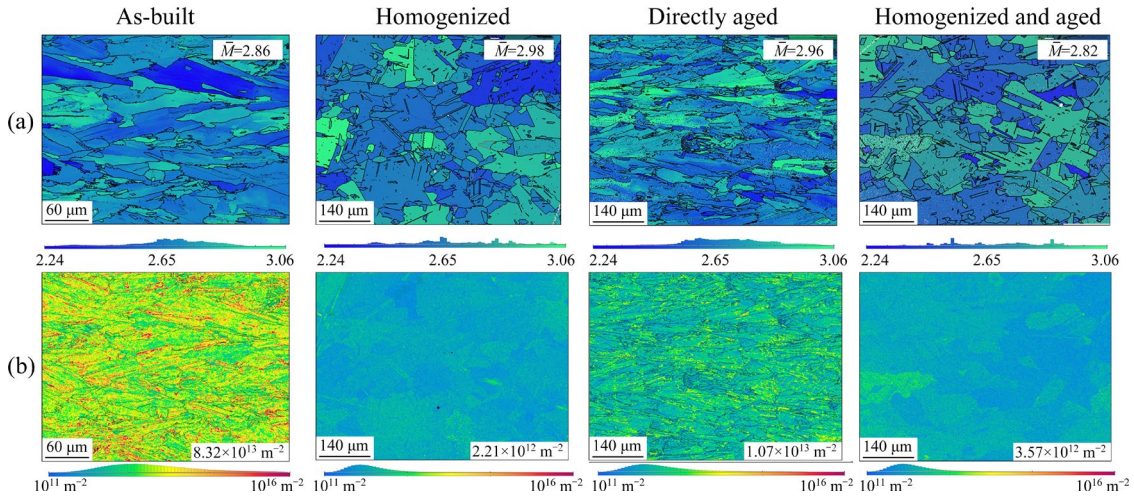

Fig. 9 Taylor factors (a) and geometric necessary dislocation (GND) maps (b) for different samples

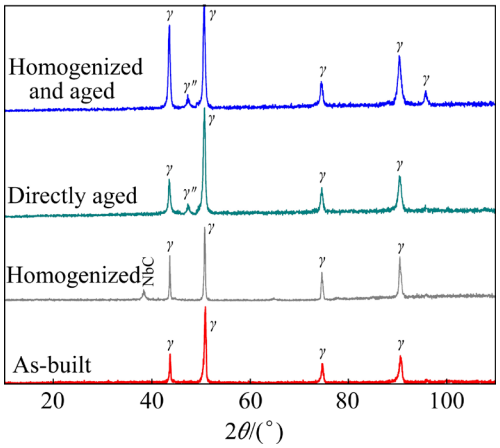

Fig. 10 XRD patterns of as-built, homogenized, directly aged, and homogenized and aged samples

homogenized, directly aged, and homogenized and aged samples were determined to be 2.8×10^{14}, 4.7×10^{12}, 1.1×10^{14}, and 6.5×10^{13} m^{-2}, respectively. These results are consistent with the dislocation density values obtained from the geometric necessary dislocation (GND) maps (Fig. 9(b)), which correspondingly resulted in dislocation strengthening of 186, 25, 122, and 88 MPa, respectively. These results demonstrate that homogenization treatment results in diminishing the dislocation density and its contribution in the total strength.

3.5.4 Solid solution strengthening

An estimation of solid solution strengthening can be made using Labusch's theory [54]. The increase in the yield stress is attributed to the presence of solute atoms that serve as impediments to the dislocation movement during slip in a binary alloy, which is governed by local lattice and modulus variation in the solid solution [54]. This methodology was further extended by GYPEN and DERUYTTERE [55,56] to incorporate strengthening that resulted from the addition of alloying elements to multi-component systems. Consequently, Eq. (5) can be used to calculate the solid solution strengthening:

$$\Delta\sigma_{ss}=(\sum\beta_i^{3/2}x_i)^{2/3} \quad (5)$$

where x_i refers to the molar fraction of element i in the FCC matrix. In addition, the value of β_i for each element is presented as follows: $\beta_i=3/2\mu(\eta_i'+16\delta_i)^{3/2}$ [51,57]. In the given equation, $\eta_i'(\eta_i'=\eta_i/(1+0.5|\eta_i|))$, where η_i is the modulus mismatch with respect to the Ni element) can be calculated based on the modulus mismatch for each element. Furthermore, δ_i represents the atomic size mismatch of elements with regard to the Ni element. These variables are calculated and shown in Table 2. It should be noted that G and r in Table 2 represent the shear modules and atomic radius of each element, respectively. Based on Table 2 and chemical composition of the austenite matrix (Table 3), the contribution of the solid solution in the yield strength of the samples was calculated to be 268 MPa for the as-built sample, 281 MPa for the homogenized sample, 231 MPa for the directly aged sample, and 199 MPa for the homogenized and aged sample.

Table 2 Variables for calculation of solid solution strengthening

Element	G/GPa	r/nm	η_i'	δ_i
Cr	115	0.125	0.408	0.067
Nb	38	0.143	0.401	0.221
Mo	120	0.136	0.45	0.164
Ti	44	0.146	0.348	0.25
Al	24	0.143	0.508	0.2237
Fe	82	0.124	0.075	0.061

Table 3 EDS analysis results from matrix

Sample	Content/at.%						
	Ni	Cr	Nb	Mo	Ti	Al	Fe
As-built	53.3	22	3.3	1.1	1.1	0.9	18.3
Homogenized	53.8	21.1	3.4	1.6	1.8	0.8	17.5
Directly aged	54.2	21.2	3.3	1	1.3	0.8	18.2
Homogenized and aged	54.6	21.5	3.2	1.4	1.2	0.9	17.2

3.5.5 Precipitation strengthening

With respect to precipitate size, there are two primary mechanisms by which precipitates resist dislocation movement. These mechanisms are known as the Orowan mechanism, where dislocations bypass precipitates, and the shearing mechanism, where dislocations cut through particles [48,50,58]. For the shearing mechanism, the main sources of precipitation strengthening are coherency strengthening and order strengthening. The coherency strain between the matrix and the precipitate results in coherency strengthening, while the formation of an antiphase boundary leads to order strengthening [48,50]. The following equations

can be employed to quantitatively evaluate how each strengthening mechanism contributes to the yield strength of IN718 alloy [48,59]:

$$\Delta\sigma_{\gamma''\text{-coherency}} = 1.7\bar{M}\mu\delta_{\gamma/\gamma''}^{3/2}\left[\frac{Rf(1-\Lambda)}{2bA^2}\right]^{1/2} \tag{6}$$

$$\Delta\sigma_{\gamma''\text{-order}} = \bar{M}\left[\frac{\gamma_{\text{APB}}}{2b}\right]\left\{\left[\frac{4\gamma_{\text{APB}}fR}{\pi T}\left(\frac{\sqrt{6}}{3A}\right)^{1/2}\right]^{1/2} - \beta f\right\} \tag{7}$$

$$\Delta\sigma_{\gamma''\text{-Orowan(plate)}} = \frac{0.85\bar{M}\mu b}{2\pi\sqrt{(1-\nu)}}\cdot \frac{\sqrt{fA}+\left(\frac{2}{\pi}-\frac{\pi}{2A}\right)fA}{2R\left(\frac{2A}{3}\right)^{1/3}\left[1-\frac{\pi}{2A}\left(\left(\sqrt{fA}\right)+\left(\frac{2}{\pi}-\frac{\pi}{2A}\right)fA\right)\right]}\cdot \ln\left[4R(2A/3)^{1/3}/(\pi r_0)\right] \tag{8}$$

$$\Delta\sigma_{\text{Laves-Orowan(rod)}} = \frac{0.85\bar{M}\mu b}{2\pi\sqrt{(1-\nu)}}\cdot \frac{1}{2\sqrt{3}R\left(\frac{2}{3A}\right)^{1/3}\left[\sqrt{\left(\frac{\pi}{6f}\right)}-\sqrt{\frac{2}{3}}\right]}\cdot \ln\left(2\sqrt{2}R\left(\frac{2}{3A}\right)^{1/3}/r_0\right) \tag{9}$$

where γ_{APB} is the antiphase boundary energy (296 mJ/m^2 for γ'' in IN718 [53]), f is the volume fraction of precipitates, R represents half of the mean length of γ'' precipitates, and $\delta_{\gamma/\gamma''}$ is the lattice misfit of γ and γ'' phases (~0.023 for IN718 [48]). Moreover, T denotes dislocation line tension ($T=\mu b^2/2$) and the Poisson ratio, denoted by ν, is equal to 0.3. The value of Λ can be either 0 or 1/3, depending on whether all the precipitates are related to a specific variant or three variants in equal numbers [53]. Additionally, A represents the aspect ratio of γ'' precipitates and r_0 represents the radius of the dislocation core, which is equal to b [59]. Based on the aspect ratio of γ'' precipitates in the directly aged and homogenized and aged samples (3.25 and 2.92, respectively) and their corresponding volume fractions (14.2% for the directly aged sample and 12.5% for the homogenized and aged sample) as well as other parameters already introduced, the coherency, order, and Orowan mechanisms were plotted as a function of R in Fig. 11 to determine which strengthening mechanism is dominant.

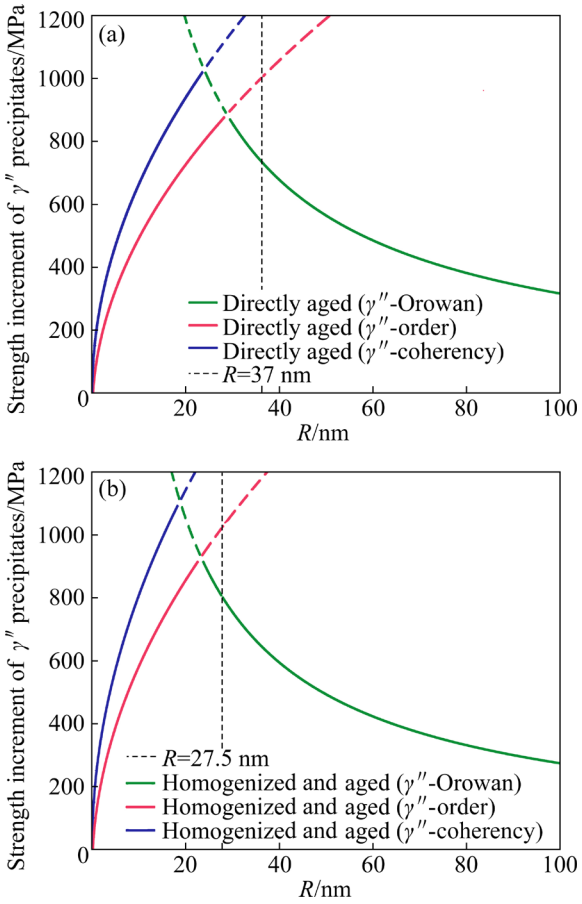

Fig. 11 Calculation of precipitation strengthening mechanisms with variation of γ'' radius: (a) Directly aged sample; (b) Homogenized and aged sample

It can be seen from Fig. 11 that in the case of directly aged sample, the critical precipitate size for the γ'' phase transitioning from the coherency mechanism to the Orowan mechanism is about 23 nm. Additionally, the critical precipitate size for the γ'' phase transitioning from the order mechanism to the Orowan mechanism is around 28 nm in the directly aged sample. In addition, the critical precipitate size of the γ'' phase from the coherency mechanism to the Orowan mechanism is estimated to be 14 nm in the case of the homogenized sample, and that of the γ'' precipitates from the order mechanism to the Orowan mechanism is around 23 nm. It is noteworthy that the findings of this study are in good agreement with those of previous studies [48].

According to Fig. 6, it is evident that the critical size of precipitates is smaller than the

measured ones in the directly aged and homogenized and aged samples (37 and 27.5 nm, respectively). Hence, it appears that the dislocation bypassing mechanism is predominant in both samples. As a result, Equation (8) was employed to determine the contribution of γ'' precipitates in the yield strength of directly aged and homogenized and aged samples. Accordingly, the strengthening of γ'' precipitates is calculated to be 740 MPa for the directly aged sample and 810 MPa for the homogenized and aged sample.

Furthermore, Eq. (9) was used to calculate the strengthening contribution of the Laves phase in the as-built and directly aged samples. Due to the absence of homogenization treatment in the directly aged sample, the Laves phase still exists in the microstructure (Fig. 6(b)) and has an impact on the obtained ductility, which is consistent with previous study [28]. Accordingly, the strengthening of Laves phase in the as-built and directly aged samples was calculated as an equal value of 98 MPa based on the volume fraction of 4.78% as well as the precipitate size of 120 nm.

It should be noted that while the NbC carbide is precipitated during homogenization treatment (Fig. 3(b)), the volume fraction of this phase is less than 0.6% [26]. Hence, the precipitation strengthening of NbC carbide can be neglected. Moreover, because the γ'' phase is the main strengthening precipitate and the amount of γ' phase is expected to be low in the heat treating conditions used in this work, the effect of γ' precipitates strengthening was also neglected.

3.5.6 Comparison of experimental and theoretical yield strength

A comparison is made between experimental yield strength and theoretical yield strength and the results are shown in Fig. 12. It can be seen that there is a good correlation between the theoretical and experimental results. Accordingly, it can be stated that the differences between the theoretical and the experimental results is less than 10%. In other words, adopting this theoretical approach confirms the experimental results of tensile behavior (Fig. 8). Moreover, it can be seen that the precipitation strengthening [60−62] plays a vital role in the enhancement of the mechanical properties in IN718 fabricated by the L-PBF method. Furthermore, it is rational to maintain high dislocation density by not performing homogenization treatment at the expense of a decrease in ductility, since the portion of dislocation strengthening is rather significant.

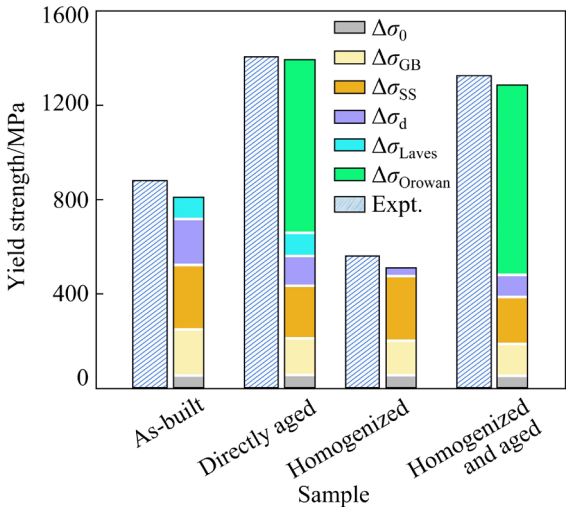

Fig. 12 Comparison of experimental and theoretical yield strengths of samples

3.6 Elevated-temperature mechanical properties

Since IN718 superalloy is intended to be used at 650 °C [31,63−65], the elevated-temperature tensile properties of this alloy at 650 °C were investigated and the resultant engineering stress−strain curves are shown in Fig. 13(a). It can be seen that YS and UTS of the as-built sample are 740 and 790 MPa, respectively. However, homogenization treatment resulted in a decrease in the YS and UTS to 430 and 484 MPa, respectively. Moreover, it can be seen that the aging treatments of both as-built and homogenized samples lead to an increase in the YS and UTS, in which the YS and UTS for the homogenized and aged sample are 1071 and 1141 MPa, respectively; while the YS and UTS for the directly aged sample are 1122 and 1192 MPa, respectively. It can be seen that the trend of YS and UTS is comparable to that of the room-temperature tensile test. However, the values of YS and UTS are lower compared to the corresponding values for the room-temperature tensile tests, which are related to the effect of deformation temperature.

The obtained creep strain−time plots for different samples under the stress of 700 MPa are shown in Fig. 13(b), and the obtained creep lives and the minimum creep rates are also summarized in Figs. 13(c) and (d), respectively. Furthermore, for conducting a comprehensive comparison, the creep data of a wrought IN718 with [66] were added to

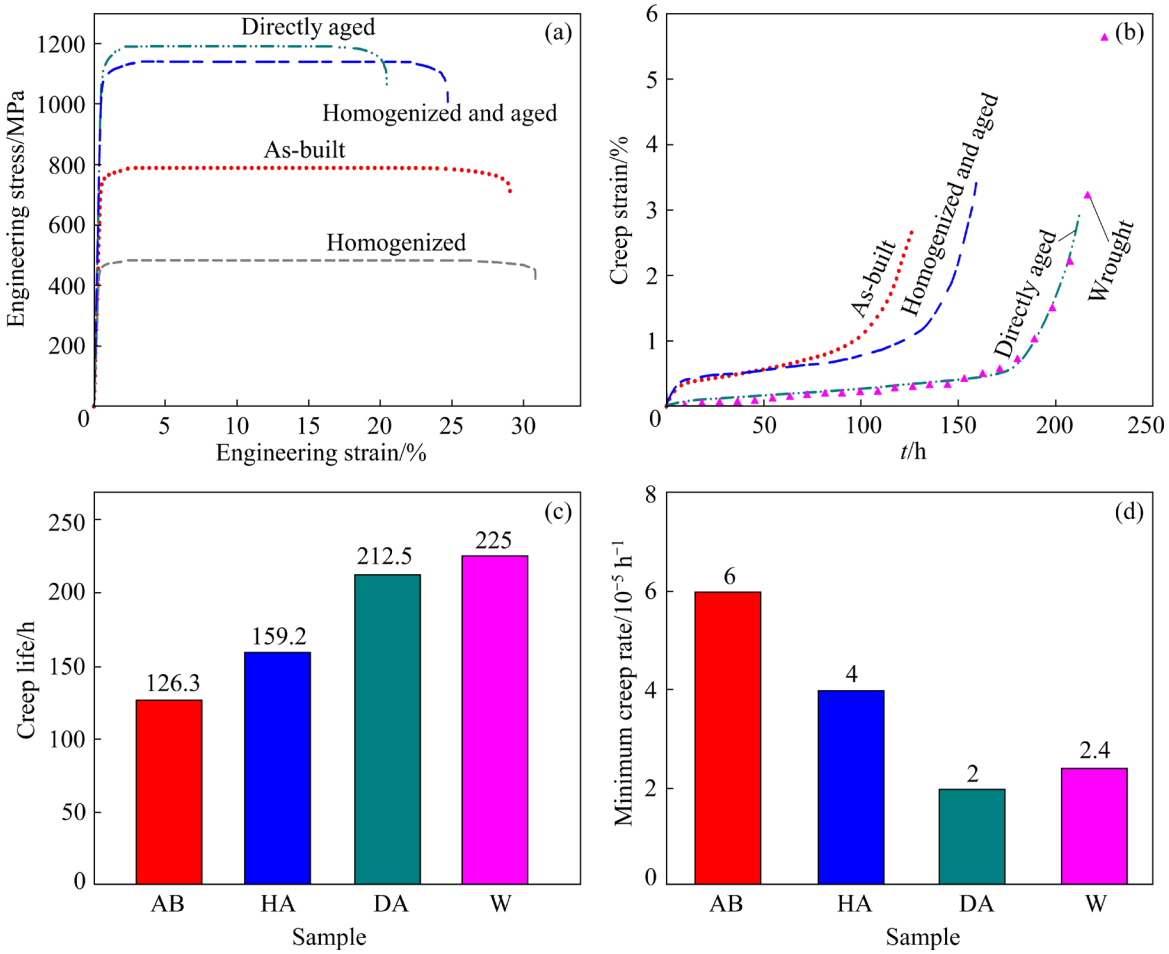

Fig. 13 Elevated-temperature engineering stress−strain curves at 650 °C (a), creep strain−time plots at 650 °C under stress of 700 MPa (b), comparison of creep lives (c), and minimum creep rates (d) of different samples (in Figs. (c) and (d), abbreviations AB, HA, DA, and W represent as-built, homogenized and aged, directly aged, and wrought samples, respectively; creep data of wrought alloy were taken from a related investigation [66] with similar test circumstances)

Figs. 13(b, c, d). It can be seen that the aging treatment resulted in an increase of creep life and a decrease of the minimum creep rate, which is related to the favorable effect of the precipitates. However, the directly aged sample shows better creep resistance compared to the homogenized and aged sample, which is related to the presence of finer and more homogeneously dispersed precipitate particles. The obtained results of the creep test are in good agreement with previous studies [45,67]. The minimum creep rates and rupture time are similar to results of MCLOUTH et al [45], who reported rupture time of 114.2 and 132.3 h for different additively manufactured Inconel 718 superalloy samples during the creep tests performed under a similar stress of 690 MPa at 650 °C. These creep lives are comparable to the value of 126.3 h for the as-built sample in Fig. 13(c).

The enhancement of creep life by performing aging treatment was also reported in a previous study [67] and confirmed the obtained results of this study. Moreover, the creep strain−time plot for the wrought IN718 after aging treatment is also shown in Fig. 13(b), which reveals that the creep resistance of the directly aged sample is comparable to the commonly used wrought IN718 superalloy. Accordingly, it can be deduced that direct aging from the as-built condition is the recommended practice to process the additively manufactured IN718 superalloy.

4 Conclusions

(1) Homogenization treatment resulted in a fast decrease of hardness at all temperatures as well as a lower absolute value. At temperatures ≥1100 °C, homogenization led to the occurrence of recrystallization, which resulted in the appearance

of equiaxed grains and diminishing of dislocation density. The grain growth was found to be sluggish during homogenization, which was attributed to the presence of grain boundary carbides.

(2) For each aging temperature, the hardness increased up to the peak-aged condition, and then decreased during overaging. Kinetics analysis showed that the required time and activation energy for reaching the peak-aged condition increased after homogenization; while direct aging treatment resulted in a faster aging response. The precipitation activation energy for the homogenized and aged condition was obtained as 203.2 kJ/mol, which is consistent with the value of 201.7 kJ/mol for the diffusion of Nb in Ni; while it is higher than the obtained value for the diffusion of Nb in IN718 superalloy fabricated by L-PBF (~160 kJ/mol).

(3) Due to the precipitation of strengthening phases, the aging treatment led to a significant improvement in the room-temperature tensile properties, in which theoretical study of strengthening mechanisms confirmed the experimental results. Moreover, since the portion of dislocation hardening was rather significant, it was found to be rational to maintain high dislocation density by neglecting the homogenization treatment at the expense of a decrease in ductility. The YS and UTS for the homogenized and aged sample were 1325 and 1473 MPa, respectively; while the YS and UTS for the directly aged sample were 1403 and 1536 MPa, respectively.

(4) The elevated-temperature tensile properties and creep behavior followed those of the room temperature tensile samples, where the direct aging treatment resulted in a higher value of UTS as well as the optimum creep life and lowest minimum creep rate in comparison with other heat treatment routes. These were attributed to the presence of fine and uniformly dispersed strengthening precipitates in conjunction with the high dislocation density.

CRediT authorship contribution statement

Sajad GHAEMIFAR: Conceptualization, Investigation, Writing – Original draft; **Milad ROOSTAEI:** Investigation, Writing − Original draft; **Mohammad REZA ZAMANI:** Investigation, Writing − Original draft; **Stefan WURSTER:** Writing − Review & editing; **Hamed MIRZADEH:** Conceptualization, Writing − Review & editing, Supervision.

Declaration of competing interest

The authors declare that they have no known competing financial interests or personal relationships that could have appeared to influence the work reported in this paper.

References

[1] SHAHWAZ M, NATH P, SEN I. A critical review on the microstructure and mechanical properties correlation of additively manufactured nickel-based superalloys [J]. Journal of Alloys and Compounds, 2022, 907: 164530.

[2] KHODASHENAS H, MIRZADEH H. Post-processing of additively manufactured high-entropy alloys—A review [J]. Journal of Materials Research and Technology, 2022, 21: 3795−3814.

[3] OSMAN H, LIN L I. Additive manufacturing of high-entropy alloy composites: A review [J]. Transactions of Nonferrous Metals Society of China, 2023, 33(1): 1−24.

[4] WU B, LIANG J J, ZHOU Y Z, YANG Y H, LI J G, SUN X F. Influence of laser power on microstructure and tensile property of a new nickel-based superalloy designed for additive manufacturing [J]. Transactions of Nonferrous Metals Society of China, 2023, 33(4): 1124−1143.

[5] KHODABAKHSHI F, HASANI N, KALAIE M R, HADADZADEH A, WELLS M A, MOHAMMADI M. Dynamic recrystallization under hot deformation of additively manufactured 316 L stainless steel [J]. Materials Characterization, 2023, 202: 113055.

[6] JAFARI D, VANEKER T H J, GIBSON I. Wire and arc additive manufacturing: Opportunities and challenges to control the quality and accuracy of manufactured parts [J]. Materials & Design, 2021, 202: 109471.

[7] SOOD A, SCHIMMEL J, FERREIRA V M, BOSMAN M, GOULAS C, POPOVICH V, HERMANS M J M. Directed energy deposition of Invar 36 alloy using cold wire pulsed gas tungsten arc welding: Effect of heat input on the microstructure and functional behavior [J]. Journal of Materials Research and Technology, 2023, 25: 6183−6197.

[8] HOSSEINI E, POPOVICH V A. A review of mechanical properties of additively manufactured Inconel 718 [J]. Additive Manufacturing, 2019, 30: 100877.

[9] ZHAO Y, XIONG W. Influence of homogenization on phase transformations during isothermal aging of Inconel 718 superalloys fabricated by additive manufacturing and suction casting [J]. Materials (Basel), 2023, 16(14): 4968.

[10] MOSTAFAEI A, ZHAO C, HE Y N, GHIAASIAAN S R, SHI B, SHAO S, SHAMSAEI N, WU Z, KOURAYTEM N, SUN T, PAUZA J. Defects and anomalies in powder bed fusion metal additive manufacturing [J]. Current Opinion in Solid State and Materials Science, 2022, 26(2): 100974.

[11] GORDON J V, NARRA S P, CUNNINGHAM R W, LIU H, CHEN H M, SUTER R M, BEUTH J L, ROLLETT A D. Defect structure process maps for laser powder bed fusion additive manufacturing [J]. Additive Manufacturing, 2020, 36: 101552.

[12] MALAKIZADI A, MALLIPEDDI D, DADBAKHSH S, M'SAOUBI R, KRAJNIK P. Post-processing of additively

manufactured metallic alloys—A review [J]. International Journal of Machine Tools and Manufacture, 2022, 179: 103908.

[13] MOTALLEBI R, SAVAEDI Z, MIRZADEH H. Post-processing heat treatment of lightweight magnesium alloys fabricated by additive manufacturing: A review [J]. Journal of Materials Research and Technology, 2022, 20: 1873−1892.

[14] SEGURA I A, MURR L E, TERRAZAS C A, BERMUDEZ D, MIRELES J, INJETI V S V, LI K, YU B, MISRA R D K, WICKER R B. Grain boundary and microstructure engineering of Inconel 690 cladding on stainless-steel 316L using electron-beam powder bed fusion additive manufacturing [J]. Journal of Materials Science & Technology, 2019, 35(2): 351−367.

[15] LIN Y C, YANG H, HE D G, CHEN J. A physically-based model considering dislocation–solute atom dynamic interactions for a nickel-based superalloy at intermediate temperatures [J]. Materials & Design, 2019, 183: 108122.

[16] AZARBARMAS M, AGHAIE-KHAFRI M, CABRERA J M, CALVO J. Dynamic recrystallization mechanisms and twining evolution during hot deformation of Inconel 718 [J]. Materials Science and Engineering: A, 2016, 678: 137−152.

[17] ATHREYA C N, DEEPAK K, KIM D I, DE BOER B, MANDAL S, SARMA V S. Role of grain boundary engineered microstructure on high temperature steam oxidation behaviour of Ni based superalloy alloy 617 [J]. Journal of Alloys and Compounds, 2019, 778: 224−233.

[18] MOSTAFAEI A, GHIAASIAAN R, HO I T, STRAYER S T, CHANG K C, SHAMSAEI N, SHAO S, PAUL S, YEH A C, TIN S, TO A C. Additive Manufacturing of nickel-based superalloys: A state-of-the-art review on process−structure−defect−property relationship [J]. Progress in Materials Science, 2023, 136: 101108.

[19] RAGHAVAN S, ZHANG B, WANG P, SUN CN, NAI M L, LI T, WEI J. Effect of different heat treatments on the microstructure and mechanical properties in selective laser melted Inconel 718 alloy [J]. Materials and Manufacturing Processes, 2017, 32(14): 1588−1595.

[20] BABU S S, RAGHAVAN N, RAPLEE J, FOSTER S J, FREDERICK C, HAINES M, DINWIDDIE R, KIRKA M K, PLOTKOWSKI A, LEE Y, DEHOFF R R. Additive manufacturing of nickel superalloys: Opportunities for innovation and challenges related to qualification [J]. Metallurgical and Materials Transactions A, 2018, 49: 3764−3780.

[21] PÁRAMO-KAÑETAS P J, OZTURK U, CALVO J, GUERRERO-MATA M P, ZAMORA-ANTUÑANO M A, CABRERA-MARRERO J M. Analysis of strain-induced precipitates by delta-processing in Inconel 718 superalloy [J]. Materials Characterization, 2021, 173: 110926.

[22] RAFIEI M, MIRZADEH H, MALEKAN M. Delta processing effects on the creep behavior of a typical Nb-bearing nickel-based superalloy [J]. Vacuum, 2021, 184: 109913.

[23] SUI S, CHEN J, LI Z, LI H S, ZHAO X, TAN H. Investigation of dissolution behavior of laves phase in inconel 718 fabricated by laser directed energy deposition [J]. Additive Manufacturing, 2020, 32: 101055.

[24] LALEH M, SADEGHI E, REVILLA R I, CHAO Q, HAGHDADI N, HUGHES A E, XU W, DE GRAEVE I, QIAN M, GIBSON I, TAN M Y. Heat treatment for metal additive manufacturing [J]. Progress in Materials Science, 2023, 133: 101051.

[25] GHAEMIFAR S, MIRZADEH H. Dissolution kinetics of Laves phase during homogenization heat treatment of additively manufactured Inconel 718 superalloy [J]. Journal of Materials Research and Technology, 2023, 24: 3491−3501.

[26] GHAEMIFAR S, MIRZADEH H. Precipitation kinetics of niobium carbide (NbC) during homogenization heat treatment of additively manufactured Inconel 718 superalloy [J]. Journal of Materials Research and Technology, 2023, 25: 1774−1781.

[27] GALLMEYER T G, MOORTHY S, KAPPES B B, MILLS M J, AMIN-AHMADI B, STEBNER A P. Knowledge of process−structure−property relationships to engineer better heat treatments for laser powder bed fusion additive manufactured Inconel 718 [J]. Additive Manufacturing, 2020, 31: 100977.

[28] HUANG W, YANG J, YANG H, JING G, WANG Z, ZENG X. Heat treatment of Inconel 718 produced by selective laser melting: Microstructure and mechanical properties [J]. Materials Science and Engineering: A, 2019, 750: 98−107.

[29] SANCHEZ S, GASPARD G, HYDE C J, ASHCROFT I A, RAVI G A, CLARE A T. On the thermomechanical aging of LPBF alloy 718 [J]. Materials Science and Engineering: A, 2022, 841: 142998.

[30] BEAUSIR B, FUNDENBERGER J J. Analysis tools for electron and X-ray diffraction [M]. Metz, France: ATEX-Softw. Univ, 2017.

[31] THOMAS A, EL-WAHABI M, CABRERA J M, PRADO J M. High temperature deformation of Inconel 718 [J]. Journal of Materials Processing Technology, 2006, 177(1/2/3): 469−472.

[32] DOĞU M N, DAVUT K, OBEIDI M A, YALÇIN M A, GU H, LOW T S, GINN J, BRABAZON D. Recrystallization and grain growth kinetics of IN718 manufactured by laser powder bed fusion [J]. Journal of Materials Research and Technology, 2022, 19: 4242−4257.

[33] AOTA L S, BAJAJ P, ZILNYK K D, JÄGLE E A, PONGE D, SANDIM H R Z, RAABE D. Recrystallization kinetics, mechanisms, and topology in alloys processed by laser powder-bed fusion: AISI 316L stainless steel as example [J]. Materialia, 2021, 20: 101236.

[34] RAFIEI M, MIRZADEH H, MALEKAN M. SOHRABI M J. Homogenization kinetics of a typical nickel-based superalloy [J]. Journal of Alloys and Compounds, 2019, 793: 277−282.

[35] ZHAO Y H, MENG F, LIU C, TAN S S, XIONG W. Impact of homogenization on microstructure−property relationships of Inconel 718 alloy prepared by laser powder bed fusion [J]. Materials Science and Engineering: A, 2021, 826: 141973.

[36] KOURAYTEM N, VARGA J, AMIN-AHMADI B, MIRMOHAMMAD H, CHANUT R A, SPEAR A D, KINGSTEDT O T. A recrystallization heat-treatment to reduce deformation anisotropy of additively manufactured Inconel 718 [J]. Materials & Design, 2021, 198: 109228.

[37] NAJAFKHANI F, KHEIRI S, POURBAHARI B, MIRZADEH H. Recent advances in the kinetics of normal/ abnormal grain growth: A review [J]. Archives of Civil and Mechanical Engineering, 2021, 21: 29.

[38] TUCHO W M, CUVILLIER P, SJOLYST-KVERNELAND A, HANSEN V. Microstructure and hardness studies of Inconel 718 manufactured by selective laser melting before and after solution heat treatment [J]. Materials Science and Engineering: A, 2017, 689: 220−232.

[39] DONACHIE M J, DONACHIE S J. Superalloys: A technical guide [M]. New York: ASM International, 2002.

[40] ZHANG S Y, WANG L L, LIN X, YANG H O, LI M H, LEI L M, HUANG W D. Precipitation behavior of δ phase and its effect on stress rupture properties of selective laser-melted Inconel 718 superalloy [J]. Composites Part B: Engineering, 2021, 224: 109202.

[41] SOHRABI M J, MIRZADEH H, MEHRANPOUR M S, HEYDARINIA A, RAZI R. Aging kinetics and mechanical properties of copper-bearing low-carbon HSLA-100 microalloyed steel [J]. Archives of Civil and Mechanical Engineering, 2019, 19(4): 1409−1418.

[42] FISHER D. A directory of Arrhenius parameters: Metals [M]. Geneva: Trans Tech Publications, 2014: 1−358.

[43] RAFIEI M, MIRZADEH H, MALEKAN M. Precipitation kinetics of γ'' phase and its mechanism in a Nb-bearing nickel-based superalloy during aging [J]. Vacuum, 2020, 178: 109456.

[44] ZHAO Y, GUAN K, YANG Z, HU Z, QIAN Z, WANG H, MA Z. The effect of subsequent heat treatment on the evolution behavior of second phase particles and mechanical properties of the Inconel 718 superalloy manufactured by selective laser melting [J]. Materials Science and Engineering: A, 2020, 794: 139931.

[45] MCLOUTH T D, WITKIN D B, BEAN G E, SITZMAN S D, ADAMS P M, LOHSER J R, YANG J M, ZALDIVAR R J. Variations in ambient and elevated temperature mechanical behavior of IN718 manufactured by selective laser melting via process parameter control [J]. Materials Science and Engineering: A, 2020, 780: 139184.

[46] ZHOU F, HU X G, ZHOU Y, XU Z, GUO C, LI G, LI Z Y, HUANG Y H, ZHU Q. Effects of post-heat treatment on anisotropic mechanical properties of laser additively manufactured IN718 [J]. Materials Science and Engineering: A, 2023, 877: 145144.

[47] SOHRABI M J, KALHOR A, MIRZADEH H, RODAK K, KIM H S. Tailoring the strengthening mechanisms of high-entropy alloys toward excellent strength−ductility synergy by metalloid silicon alloying: A review [J]. Progress in Materials Science, 2024, 144: 101295.

[48] ZHANG S Y, LIN X, WANG L L, YU X B, HU Y L, YANG H O, LEI L M, HUANG W D. Strengthening mechanisms in selective laser-melted Inconel 718 superalloy [J]. Materials Science and Engineering: A, 2021, 812: 141145.

[49] KIM S, CHOI H, LEE J, KIM S. Room and elevated temperature fatigue crack propagation behavior of Inconel 718 alloy fabricated by laser powder bed fusion [J]. International Journal of Fatigue, 2020, 140: 105802.

[50] SUI S, TAN H, CHEN J, ZHONG C L, LI Z, FAN W, GASSER A, HUANG W D. The influence of Laves phases on the room temperature tensile properties of Inconel 718 fabricated by powder feeding laser additive manufacturing [J]. Acta Materialia, 2019, 164: 413−427.

[51] GALINDO-NAVA E I, CONNOR L D, RAE C M F. On the prediction of the yield stress of unimodal and multimodal γ' nickel-base superalloys [J]. Acta Materialia, 2015, 98: 377−390.

[52] MA K K, WEN H M, HU T, TOPPING T D, ISHEIM D, SEIDMAN D N, LAVERNIA E J, SCHOENUNG J M. Mechanical behavior and strengthening mechanisms in ultrafine grain precipitation-strengthened aluminum alloy [J]. Acta Materialia, 2014, 62: 141−155.

[53] OBLAK J M, PAULONIS D F, DUVALL D S. Coherency strengthening in Ni base alloys hardened by DO22 γ' precipitates [J]. Metallurgical and Materials Transactions B, 1974, 5: 143−153.

[54] LABUSCH R. A statistical theory of solid solution hardening [J]. Physica Status Solidi (b), 1970, 41(2): 659−669.

[55] GYPEN L A, DERUYTTERE A. Multi-component solid solution hardening: Part 1. Proposed model [J]. Journal of Materials Science, 1977, 12: 1028−1033.

[56] GYPEN L A, DERUYTTERE A. Multi-component solid solution hardening: Part 2. Agreement with experimental results [J]. Journal of Materials Science, 1977, 12: 1034−1038.

[57] FISHER J C. On the strength of solid solution alloys [J]. Acta Metallurgica, 1954, 2(1): 9−10.

[58] ZAMANI M R, ROOSTAEI M, MIRZADEH H, MALEKAN M, SONG M. Tailoring the microstructure and mechanical properties of $(CrMnFeCoNi)_{100-x}C_x$ high-entropy alloys: Machine learning, experimental validation, and mathematical modeling [J]. Current Opinion in Solid State and Materials Science, 2023, 27(5): 101105.

[59] SUN P F, YAN N, WEI S, WANG D Z, SONG W J, TANG C W, YANG J X, XU Z D, HU Q W, ZENG X Y. Microstructural evolution and strengthening mechanisms of Inconel 718 alloy with different W addition fabricated by laser cladding [J]. Materials Science and Engineering: A, 2023, 868: 144535.

[60] ZAMANI M R, MIRZADEH H, MALEKAN M, WEIßENSTEINER I, ROOSTAEI M. Unveiling the strengthening mechanisms of as-cast micro-alloyed CrMnFeCoNi high-entropy alloys [J]. Journal of Alloys and Compounds, 2023, 957: 170443.

[61] RAFIEI M, MIRZADEH H, MALEKAN M. Micro-mechanisms and precipitation kinetics of delta (δ) phase in Inconel 718 superalloy during aging [J]. Journal of Alloys and Compounds, 2019, 795: 207−212.

[62] MIRZADEH H. Quantification of the strengthening effect of reinforcements during hot deformation of aluminum-based composites [J]. Materials & Design, 2015, 65: 80−82.

[63] GAO P, ZHANG K F, ZHANG B G, JIANG S S, ZHANG B W. Microstructures and high temperature mechanical properties of electron beam welded Inconel 718 superalloy thick plate [J]. Transactions of Nonferrous Metals Society of China, 2011, 21(suppl.): 315−322.

[64] DENG D W, WANG C G, LIU Q Q, NIU T T. Effect of standard heat treatment on microstructure and properties of borided Inconel 718 [J]. Transactions of Nonferrous Metals Society of China, 2015, 25(2): 437−443.

[65] CHAI L J, YUAN S S, HUANG W J, YANG X S, WANG F J, WANG D Z, WANG J J. Microstructural characterization of Inconel 718 alloy after pulsed laser surface treatment at

different powers [J]. Transactions of Nonferrous Metals Society of China, 2018, 28(8): 1530−1537.
[66] SUGAHARA T, MARTINOLLI K, REIS D A P, de MOURA NETO C, COUTO A A, NETO F P, BARBOZA M J R. Creep behavior of the Inconel 718 superalloy [J]. Defect and Diffusion Forum, 2012, 326/327/328: 509−514.
[67] KUO Y L, HORIKAWA S, KAKEHI K. Effects of build direction and heat treatment on creep properties of Ni-base superalloy built up by additive manufacturing [J]. Scripta Materialia, 2017, 129: 74−78.

后热处理调控增材制造 Inconel 718 高温合金的显微组织、拉伸性能和抗蠕变性能

Sajad GHAEMIFAR[1], Milad ROOSTAEI[2,3],
Mohammad REZA ZAMANI[1], Stefan WURSTER[2], Hamed MIRZADEH[1]

1. School of Metallurgy and Materials Engineering, College of Engineering, University of Tehran, Tehran, Iran;
2. Erich Schmid Institute of Materials Science, Austrian Academy of Sciences, Jahnstraße 12, 8700 Leoben, Austria;
3. Department of Materials Science, Chair of Materials Physics, Montanuniversität Leoben, 8700 Leoben, Austria

摘　要：研究了后热处理工艺对增材制造 Inconel 718 镍基合金显微组织、时效动力学和室温/高温力学性能的影响。采用扫描电子显微镜、电子背散射衍射、X 射线衍射进行表征，并测试材料的硬度、拉伸和抗蠕变性能。在高于 1100 ℃的温度下均匀化处理导致再结晶发生、位错密度减少，从而出现等轴晶粒。对于经过均匀化时效处理的 IN718 高温合金，其析出激活能为 203 kJ/mol，高于初始打印态的约 160 kJ/mol。因此，直接时效导致更快的时效响应，从而显著提升了拉伸性能，这可以用强化机制来解释。与其他热处理工艺相比，经直接时效处理后材料具有更高的高温极限抗拉强度(UTS)、最优蠕变寿命和最小蠕变速率，这源于细小且均匀分散的强化析出相与高位错密度的协同作用。

关键词：Inconel 718 高温合金；增材制造；后热处理；力学性能；抗蠕变性能

(Edited by Wei-ping CHEN)